Measurement of the absolute and differential cross sections for ^{7}Li$(\gamma, n_0)^6$Li

W. A. Wurtz* and R. E. Pywell†
Department of Physics and Engineering Physics, University of Saskatchewan, Saskatoon, Saskatchewan, Canada S7N 5E2

B. E. Norum and S. Kucuker
Department of Physics, University of Virginia, Charlottesville, Virginia 22904-4714, USA

B. D. Sawatzky
Temple University/Jefferson Laboratory, Newport News, Virginia 23606, USA

H. R. Weller, M. W. Ahmed, and S. Stave
Triangle Universities Nuclear Laboratory, Duke University, Durham, North Carolina 27708-0308, USA
(Received 13 July 2011; published 3 October 2011)

We have measured the cross section of the photoneutron reaction channel $^7\text{Li} + \gamma \rightarrow {}^6\text{Li(g.s.)} + n$ where the progeny nucleus is the ground state of ^{6}Li. We obtained the absolute cross section at photon energies 10, 11, 12, 13, 15, 20, 25, 30, and 35 MeV and also the dependence of the cross section on polar angle for all but the highest photon energy. For the energies 10 to 15 MeV we were able to use linearly polarized photons to obtain the dependence of the cross section on the photon polarization.

DOI: 10.1103/PhysRevC.84.044601 PACS number(s): 24.30.Cz, 24.70.+s, 25.10.+s, 25.20.Dc

I. INTRODUCTION

We have experimentally studied the photoneutron reaction channel $^7\text{Li} + \gamma \rightarrow {}^6\text{Li(g.s.)} + n$, which we label (γ, n_0), by making a measurement of its differential cross section. The purpose of this measurement is to supply data for comparison to theoretical calculations. For instance, the Lorentz integral transform method [1] has been applied to the total photodisintegration cross sections of the $A \leqslant 7$ nuclei [2] and to the individual photoneutron and photoproton reaction channels of ^{4}He [3]. Such calculations may use various formulations of the nucleon-nucleon interaction. Sufficiently precise experimental results can differentiate between nucleon-nucleon interactions and therefore shed light on the underlying nuclear dynamics. However, a lack of experimental data makes comparisons to calculations for specific reaction channels impossible for nuclei with $A > 4$.

Since it is not possible to completely isolate neutrons from the photoneutron reaction channels of ^{6}Li, because of the immediate decay of the highly unstable $A = 5$ progeny nuclei to the α particle [4], we find that ^{7}Li is the lightest stable nucleus with $A > 4$ for which we can isolate the photoneutron reaction channel.

II. EXPERIMENT AND ANALYSIS

A series of measurements on the lithium isotopes were performed at the High Intensity Gamma-Ray Source (HIGS) [5] at Duke University in Durham, NC, USA. HIGS is able to produce a nearly monochromatic polarized photon beam through the process of Compton backscattering. For our measurements at photon energies of 10, 11, 12, 13, and 15 MeV, we used linearly polarized photons and we were able to obtain the dependence of the cross section on photon polarization. For photon energies of 20, 25, 30, and 35 MeV, linearly polarized photons were unavailable at the time of measurement, so circularly polarized photons were used instead. As HIGS employs a synchrotron, the inherently bunched electron beam creates a time structure in the photon beam. The photon beam is macroscopically continuous but photons arrive in bunches 180 ns apart. Photon rates of up to 1×10^7 photons/s were used in these measurements.

Neutrons created by photodisintegration reactions were detected using the Blowfish Neutron Detector Array, also known simply as Blowfish [6]. Blowfish is a segmented fast-neutron detector based on 88 scintillating cells. It has a radius of 40.6 cm and has an angular acceptance of approximately 1/4 of 4π sr. The cells are filled with the liquid scintillator BC505 and their light-output characteristics are described in detail in another paper [7]. Along with scaler information for diagnostic purposes and flux normalization, three types of spectra are obtained from Blowfish. From each of the 88 cells we can obtain light output, time-of-flight (TOF), and pulse shape discrimination (PSD) spectra.

The TOF spectra record the time difference between a signal from an accelerator beam-position monitor (the arrival time of a photon bunch is given by this signal) and the signal from each cell. The TOF spectra are useful for eliminating photons that are Compton scattered from the target into the detectors. These photons will arrive before any neutrons, leaving only photons from the room background in our spectra, and these can be easily dealt with using the PSD spectra.

The PSD spectra are created by comparing the pulse from the detector, integrated over the full pulse, with one that is integrated over only the beginning of the pulse. Since recoiling

*Present address: Canadian Light Source, Saskatoon, Saskatchewan, Canada; ward.wurtz@usask.ca
†rob.pywell@usask.ca; http://nucleus.usask.ca

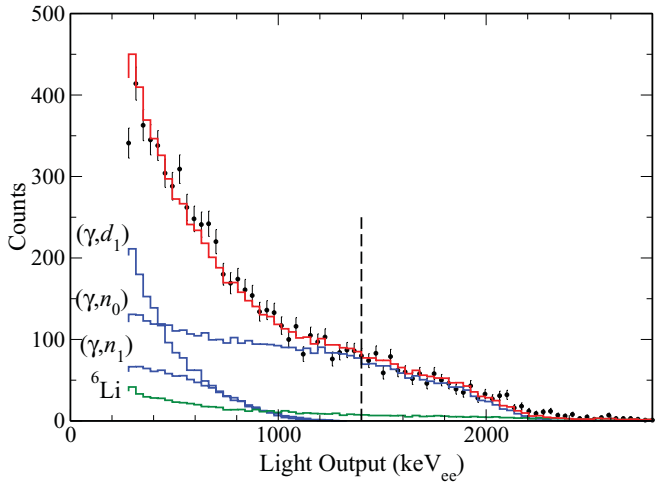

FIG. 1. (Color online) The light-output spectrum from one BC-505 Blowfish cell at a photon energy of 13 MeV with the natural lithium target in place. The data are shown by the solid circles with error bars. The histogram passing through the data points (red online) is the GEANT4 simulation result for the sum of all reaction channels plus the measured contribution from the ^{6}Li in the target. The ^{6}Li contribution is shown by the labeled histogram (green online). The simulated contribution from the significant reaction channels at this energy are shown by the labeled histograms (blue online). Note that above a light output of 1400 keV$_{ee}$, shown by the vertical dashed line, there is no contribution from any reaction channel other than the (γ, n_0) channel, after subtraction of the ^{6}Li contribution. Error bars represent statistical uncertainty only.

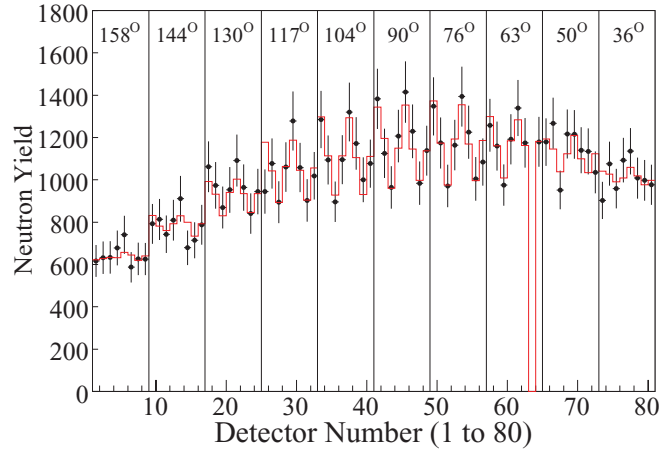

FIG. 3. (Color online) Neutron yields for Blowfish's detectors used in the analysis at a photon energy of 13 MeV. The data points are the measured yields, and the histogram (red online) represents our fit to the data. Error bars represent both systematic and statistical uncertainties added in quadrature. There are eight detectors at each polar angle, and the angle is shown on the plot with vertical lines dividing detectors at different angles. Detectors at specific polar angles are either on, perpendicular to, or at 45° to the plane of polarization. Note that detector no. 63 is omitted due to technical issues with that detector, and the detectors at angle 22° are also omitted as they did not function reliably because of the large number of γ rays scattered into them at such a shallow angle.

electrons and protons in the scintillator create pulses with different shapes, we can determine whether a photon or a neutron was detected.

A complete analysis of the Blowfish data will include all possible reaction channels that produce neutrons. A GEANT4 simulation [8] for each reaction channel can be fitted to the TOF data to extract the cross section for each reaction channel. This more complex analysis will be reported in a later publication. However, the (γ,n_0) reaction channel can be extracted without resorting to such a fit. Because Blowfish has a short flight path between the target and the neutron detector cells (406 mm), the TOF spectrum does not have sufficient resolution to unambiguously identify the (γ,n_0) neutrons. Therefore, we use the light-output spectra to eliminate neutrons from other reaction channels.

Figure 1 shows the light-output spectrum from one particular Blowfish detector cell for a photon energy of 13 MeV.

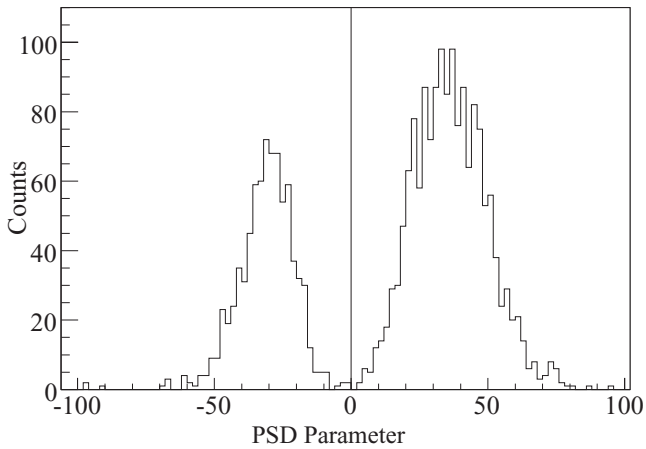

FIG. 2. Example PSD parameter histogram for a Blowfish neutron detector cell taken with a photon beam energy of 13 MeV. A light-output threshold of 1400 keV$_{ee}$ has been applied to these data. γ rays have a negative PSD parameter while neutrons have a positive PSD parameter. There is a clear separation between the two.

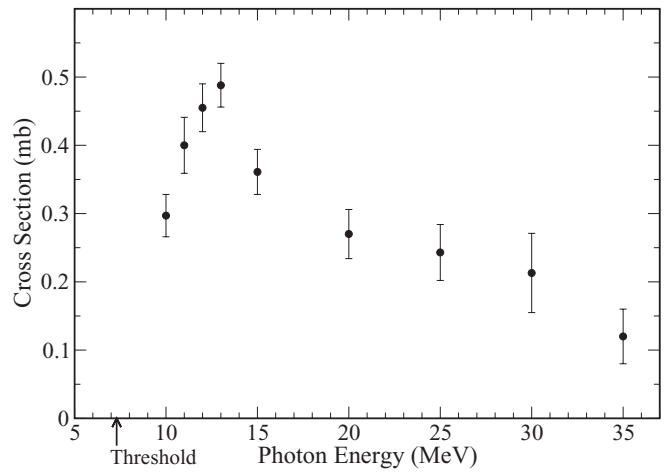

FIG. 4. The absolute cross section for $^7\mathrm{Li} + \gamma \rightarrow {}^6\mathrm{Li(g.s.)} + n$. Error bars represent both statistical and systematic uncertainties added in quadrature.

TABLE I. Absolute cross section for the reaction channel $^7\mathrm{Li} + \gamma \rightarrow {}^6\mathrm{Li(g.s.)} + n$. The first uncertainty is statistical and the second is systematic.

Energy (MeV)	Cross section (mb)
10	$0.297 \pm 0.010 \pm 0.029$
11	$0.400 \pm 0.005 \pm 0.041$
12	$0.455 \pm 0.007 \pm 0.034$
13	$0.488 \pm 0.009 \pm 0.031$
15	$0.361 \pm 0.012 \pm 0.031$
20	$0.270 \pm 0.003 \pm 0.035$
25	$0.243 \pm 0.004 \pm 0.039$
30	$0.213 \pm 0.005 \pm 0.057$
35	$0.120 \pm 0.003 \pm 0.040$

In this example it can be seen that above a light output of 1400 $\mathrm{keV_{ee}}$ (equivalent electron energy) there is no contribution (after subtracting the ^{6}Li contribution) to the spectrum from any reaction channel except the (γ,n_0) channel. The other significant reaction channels at this energy are the $^7\mathrm{Li} + \gamma \rightarrow {}^6\mathrm{Li}(2.19) + n$ channel, labeled (γ, n_1), and the $^7\mathrm{Li} + \gamma \rightarrow {}^5\mathrm{He}(1.27) + d \rightarrow {}^4\mathrm{He(g.s.)} + n + d$ reaction channel, labeled (γ, d_1). These other reaction channels can be eliminated using a simple cut on the light-output spectra. Use of such a high light-output threshold significantly reduces the efficiency of the neutron detectors and increases the statistical uncertainty of the results. However, the elimination of the need for modeling and fitting the other reaction channels greatly reduces the systematic uncertainties in the extraction of the (γ,n_0) cross section.

In addition, the high light-output threshold renders the PSD discrimination essentially 100% effective, thus eliminating photon background completely. An example PSD parameter histogram is shown in Fig. 2 with the γ rays clearly separated from the neutrons.

The photon flux is determined in two ways. First, we employ a flux monitor using five scintillating paddles [9]. Each paddle produces an analog output proportional to the light output of a scintillator. These are digitized and used in coincidence to determine photon events, which may be counted by a scaler. The dead time of our system is accounted for by gating all scalers with the system live time. This flux monitor is calibrated against a sodium iodide detector to provide an absolute photon flux. This monitor was only available for measurements at photon energies from 20 to 35 MeV. Second, we use the photons scattered from the target and into the neutron detectors of Blowfish to obtain the flux multiplied with the target length. This method was employed at all photon energies.

The target used in this experiment is natural lithium cast in a protective Teflon cylinder. Natural lithium contains $(7.56 \pm 0.04)\%$ ^{6}Li [10]. We subtract the contribution of the ^{6}Li by using measurements obtained from an isotopically enriched ^{6}Li target in an identical geometry. These measurements were made either immediately before or immediately after the ^{7}Li measurements to ensure that experimental conditions remained the same. By making a relative flux measurement between the ^{6}Li and ^{7}Li runs, we are able to directly subtract the ^{6}Li contribution from our ^{7}Li spectra. A three-paddle, scintillating flux monitor provided by HIGS was used to normalize the flux of the two measurements. This flux monitor is useful for relative flux normalization but not absolute flux determination.

An empty target container was used for background measurements with the beam. We find that the thin target windows produce negligible background neutrons but the atmospheric nitrogen produces significant numbers of neutrons. Because of the high threshold for the photodisintegration of nitrogen, these neutrons are eliminated by the light output cut.

In order to account for the finite geometry of our apparatus, we use a GEANT4 simulation for comparison. We have studied the light output of our detectors using GEANT4 [7], and the energy spectra of the neutrons produced by photodisintegration are simple to derive from relativistic kinematics. This simulation accounts for neutrons scattering from any mass in our detector geometry, including the target, the target mounts, the detectors, the detector light guides, and the detector mounts.

We use the associated Legendre function expansion

$$\frac{d\sigma}{d\Omega}(\theta,\phi) = \frac{\sigma}{4\pi}\left[1 + \sum_{k=1}^{\infty} a_k P_k^0(\cos\theta) + \sum_{k=2}^{\infty} e_k P_k^2(\cos\theta)\cos 2\phi\right],$$

TABLE II. Associated Legendre polynomial expansion coefficients a_k for the reaction channel $^7\mathrm{Li} + \gamma \rightarrow {}^6\mathrm{Li(g.s.)} + n$. The first uncertainty is statistical and the second is systematic. Only two significant figures are shown for 30 MeV due to the greater uncertainties at this energy.

Energy (MeV)	a_1	a_2	a_3	a_4
10	$-0.330 \pm 0.012 \pm 0.036$	$0.084 \pm 0.018 \pm 0.052$	$0.191 \pm 0.022 \pm 0.063$	$-0.001 \pm 0.029 \pm 0.086$
11	$-0.043 \pm 0.006 \pm 0.016$	$0.013 \pm 0.009 \pm 0.025$	$0.068 \pm 0.011 \pm 0.032$	$-0.014 \pm 0.013 \pm 0.039$
12	$-0.018 \pm 0.004 \pm 0.012$	$-0.081 \pm 0.007 \pm 0.022$	$0.043 \pm 0.008 \pm 0.026$	$-0.031 \pm 0.011 \pm 0.035$
13	$-0.044 \pm 0.005 \pm 0.016$	$-0.219 \pm 0.008 \pm 0.026$	$0.035 \pm 0.009 \pm 0.031$	$-0.025 \pm 0.012 \pm 0.042$
15	$0.016 \pm 0.005 \pm 0.017$	$-0.279 \pm 0.009 \pm 0.026$	$0.041 \pm 0.012 \pm 0.033$	$-0.038 \pm 0.014 \pm 0.042$
20	$-0.027 \pm 0.007 \pm 0.023$	$-0.417 \pm 0.014 \pm 0.046$	$-0.032 \pm 0.016 \pm 0.059$	$-0.116 \pm 0.021 \pm 0.077$
25	$-0.097 \pm 0.016 \pm 0.061$	$-0.456 \pm 0.025 \pm 0.095$	$0.180 \pm 0.032 \pm 0.140$	$-0.070 \pm 0.038 \pm 0.160$
30	$-0.02 \pm 0.04 \pm 0.12$	$-0.76 \pm 0.06 \pm 0.19$	$-0.29 \pm 0.07 \pm 0.28$	$-0.35 \pm 0.07 \pm 0.32$

TABLE III. Associated Legendre polynomial expansion coefficients e_k for the reaction channel $^7\mathrm{Li} + \gamma \rightarrow {}^6\mathrm{Li(g.s.)} + n$. The first uncertainty is statistical and the second is systematic.

Energy (MeV)	e_2	e_3	e_4
10	$-0.082 \pm 0.004 \pm 0.012$	$-0.011 \pm 0.002 \pm 0.006$	$0.004 \pm 0.001 \pm 0.004$
11	$-0.071 \pm 0.002 \pm 0.005$	$-0.002 \pm 0.001 \pm 0.003$	$-0.003 \pm 0.001 \pm 0.002$
12	$0.012 \pm 0.002 \pm 0.005$	$-0.001 \pm 0.001 \pm 0.001$	$-0.002 \pm 0.001 \pm 0.002$
13	$0.063 \pm 0.002 \pm 0.006$	$-0.003 \pm 0.001 \pm 0.002$	$-0.002 \pm 0.001 \pm 0.002$
15	$0.136 \pm 0.002 \pm 0.006$	$-0.001 \pm 0.001 \pm 0.003$	$0.000 \pm 0.001 \pm 0.002$

where P_k^q are the associate Legendre functions and a_k and e_k are their coefficients. θ is the polar angle and ϕ is the angle from the polarization vector. The quantity σ is the total cross section, while $d\sigma/d\Omega$ is the differential cross section. For this measurement we were able to obtain σ for all photon energies a_k, with $k \leqslant 4$ for all but the highest photon energy, and e_k, with $k \leqslant 4$ for photon energies $\leqslant 15$ MeV.

We determine the associated Legendre function coefficients by performing eight simulations using the uniform distribution and distributions with each of the seven a_k and e_k values alone, with all other coefficients set to zero. We use the simulation to determine each cell's neutron yield and we fit these to the measured neutron yields by adjusting a_k and e_k.

Such a fitting procedure yields an uncertainty in each a_k and e_k, which depends on the uncertainties in the cell yields. These yields have a statistical uncertainty depending on the number of counts passing the light-output cut and a contribution from the subtraction of the ^{6}Li contribution. The yields also have a systematic uncertainty which depends on our knowledge of the neutron detector cell gains, since that determines our knowledge of the light-output cut used in the simulation. There are also systematic uncertainties associated with the accuracy of our knowledge of the target and detector geometry. Because of the high light-output cuts used to separate the (γ, n_0) neutrons in this analysis, the light-output cut uncertainty has a large effect on the detector efficiency. Therefore, this is the dominant component of the systematic uncertainty for each cell. Because each of the 88 Blowfish cells will have a gain uncertainty that is largely uncorrelated to the uncertainty of other cells, the detector efficiency uncertainties will have an approximately Gaussian distribution. It is therefore appropriate to combine the statistical and systematic uncertainties for each cell in quadrature for the purposes of fitting to obtain the Legendre polynomial coefficients. The uncertainties obtained in this way were checked by performing two additional fits: one using only the statistical cell uncertainties, and the other using only the systematic cell uncertainties. When these uncertainties are combined in quadrature they yield the same values obtained using a fit with the neutron cell statistical and systematic uncertainties combined in quadrature. The result of such a fit is shown in Fig. 3. Notice that the histogram goes through nearly all the error bars, indicating that we may have overestimated our uncertainties. This is confirmed by reduced χ^2 values, which are typically less than unity. However, we feel that our uncertainties are realistic and choose not to artificially decrease the uncertainties in our neutron yields.

The fit to determine the Legendre coefficients also results in a total yield that can be used to obtain the total absolute cross section σ. The systematic uncertainty in the absolute cross section includes the uncertainties in the incident photon flux and target thickness. In general, the systematic uncertainties are three to four times larger than the statistical uncertainties.

III. RESULTS

The absolute cross section is plotted in Fig. 4 and listed in Table I. The cross section shows a sharp increase after the 7.3 MeV threshold, a peak between photon energies of 12 and

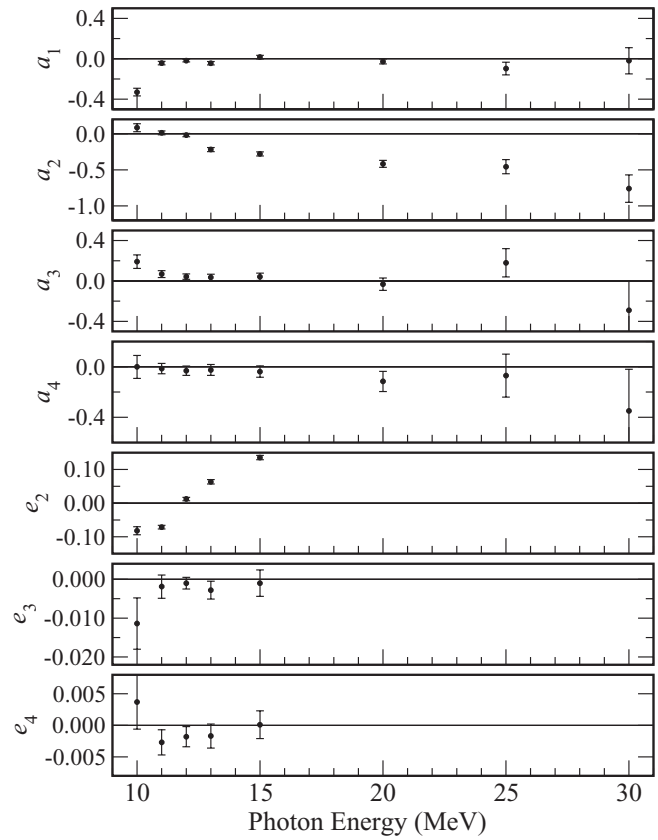

FIG. 5. Associated Legendre function coefficients for the reaction channel $^7\mathrm{Li} + \gamma \rightarrow {}^6\mathrm{Li(g.s.)} + n$. Error bars represent both statistical and systematic uncertainties added in quadrature.

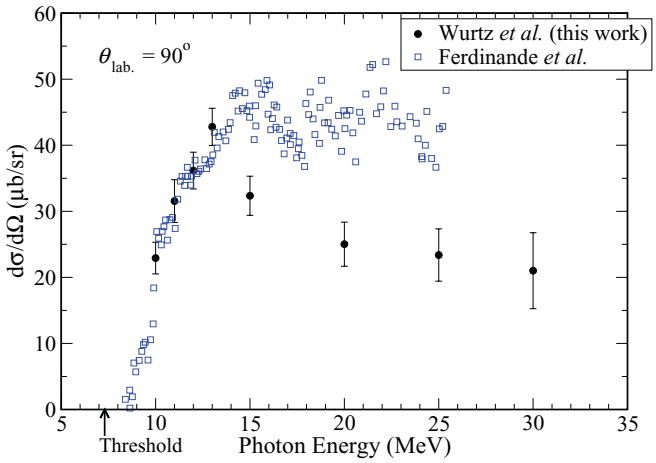

FIG. 6. (Color online) The differential cross section for $^7\mathrm{Li} + \gamma \rightarrow {}^6\mathrm{Li(g.s.)} + n$ at $\theta_{\mathrm{lab}} = 90^\circ$ from our data (closed circles) compared with that of Ferdinande *et al.* [14] (open squares). No uncertainties are reported by Ferdinande *et al*. Our error bars represent both statistical and systematic uncertainties added in quadrature.

15 MeV, and then a long, declining tail up to 35 MeV, where our data end. It was not possible to take data at lower energies as the emitted neutrons have too little kinetic energy and would fall below the detector threshold. At a photon energy of 35 MeV the uncertainties in the neutron yields of each detector cell become large, as not many neutrons survive the light-output cut required to separate the (γ,n_0) reaction channel from all others. Therefore, at that energy, we are able to obtain an absolute cross section, but we are not able to obtain the angular dependence.

The associated Legendre function coefficients with $k \leqslant 4$, with a_k values for photon energies between 10 and 30 MeV and e_k values between 10 and 15 MeV, are presented in Tables II and III, and are plotted in Fig. 5. The a_1, a_3, a_4, e_3, and e_4 coefficients are indistinguishable from zero at all photon energies except 10 MeV. The a_2 and e_2 values have definite dependence on energy and both cross zero near 12 MeV.

We have made no assumptions about which transition matrix elements (TMEs) contribute to the cross section. Therefore, we have placed no restrictions on the associated Legendre function coefficients in the fit. Under the assumption that p-wave $E1$ absorption is dominant along with contributions from s-wave $M1$ and d-wave $E2$, and that the TME amplitudes are the same for different p-wave and d-wave amplitudes, it can be shown [11–13] that $a_1 = -a_3, a_3 = -6e_3, a_4 = -12e_3$, and $a_2 \approx -2e_2$. Our results are consistent with all these relationships at all energies when systematic uncertainties are taken into account. The one exception is at 11 MeV, where the quantity $a_2 + 2e_2$ is more than four standard deviations away from the expected value of zero.

There is one previous experimental result that can provide an interesting comparison with our measurements. Ferdinande *et al.* [14] measured the differential cross section of this reaction channel at the laboratory angle $\theta_{\mathrm{lab}} = 90^\circ$ for photon energies from threshold up to 25 MeV.

Using our measured absolute cross section and Legendre coefficient values, we can compute the $\theta_{\mathrm{lab}} = 90^\circ$ differential cross section to compare with their results. The comparison is shown in Fig. 6, and we see good agreement at lower photon energies. At 15 MeV and above, the data sets disagree; our cross section decreases while the cross section of Ferdinande *et al.* stays approximately constant with increasing uncertainties. A systematic uncertainty is not quoted by Ferdinande *et al.*, and we assume that the scatter in the data points represents the statistical uncertainty. The data are a compilation of the 2-MeV-wide end-point sections of the neutron energy spectrum from bremsstrahlung beams generated by electron beam energies between 13 and 25 MeV in 2-MeV steps. Since ^{6}Li's first excited state is at 2.22 MeV, these 2-MeV end-point sections are supposed to include neutrons from only the (γ,n_0) reaction channel. However, the authors quote that the electron beam had an 8% full energy spread. This means that at higher energies it is possible that neutrons from the (γ, n_1) channel will contaminate the 2-MeV-wide end-point regions and therefore be misidentified as (γ, n_0) neutrons. This is a possible explanation for why the Ferdinande *et al.* result appears to overestimate the (γ, n_0) cross section compared to our results at energies exceeding 13 MeV.

IV. CONCLUSION

We have presented a measurements of the reaction channel $^7\mathrm{Li} + \gamma \rightarrow {}^6\mathrm{Li(g.s.)} + n$. It is our understanding that this is the first measurement of the absolute and differential cross sections of this reaction channel. It is hoped that these data, along with data from other neutron-producing reaction channels to be reported later, will prompt theoretical calculations. The comparison of such calculations with these data will provide a testing ground for nucleon-nucleon interaction formulations.

ACKNOWLEDGMENTS

We acknowledge the financial support of the Natural Sciences and Engineering Research Council of Canada (NSERC). This research was enabled by the use of computing resources provided by WestGrid and Compute/Calcul Canada. We thank Johannes Vogt and the staff of the Canadian Light Source for their help in constructing the lithium targets. We also thank the staff of the High Intensity Gamma-Ray Source for their collaboration and the excellent operation of the accelerator. This work comprises part of Wurtz's thesis [4].

[1] V. D. Efros, W. Leidemann, and G. Orlandini, Phys. Lett. B **338**, 130 (1994).

[2] V. D. Efros, W. Leidemann, G. Orlandini, and N. Barnea, J. Phys. G **34**, R459 (2007).

[3] S. Quaglioni, W. Leidemann, G. Orlandini, N. Barnea, and V. D. Efros, Phys. Rev. C: Nucl. Phys. **69**, 044002 (2004).

[4] W. A. Wurtz, Ph.D. thesis, University of Saskatchewan, 2010.

[5] V. N. Litvinenko *et al*., Phys. Rev. Lett. **78**, 4569 (1997).
[6] B. D. Sawatzky, Ph.D. Dissertation, University of Virginia, 2005.
[7] R. Pywell, B. Sawatzky, J. Ives, N. Kolb, R. Igarashi, and W. Wurtz, Nucl. Instrum. Methods Phys. Res., Sect. A **565**, 725 (2006).
[8] S. Agostinelli *et al*., Nucl. Instrum. Methods Phys. Res., Sect. A **506**, 250 (2003).
[9] R. Pywell, O. Mavrichi, W. Wurtz, and R. Wilson, Nucl. Instrum. Methods Phys. Res., Sect. A **606**, 517 (2009).
[10] J. R. de Laeter, J. K. Böhlke, P. D. Bièvre, H. Hidaka, H. S. Peiser, K. J. R. Rosman, and P. D. P. Taylor, Pure Appl. Chem. **75**, 683 (2003).
[11] H. R. Weller, J. Langenbrunner, R. M. Chasteler, E. L. Tomusiak, J. Asai, R. G. Seyler, and D. R. Lehman, At. Data Nucl. Data Tables **50**, 29 (1992).
[12] H. R. Weller, R. M. Chasteler, B. S. Marks, R. G. Seyler, and D. R. Lehman, At. Data Nucl. Data Tables **58**, 219 (1994).
[13] M. Blackston, Ph.D. thesis, Duke University, 2007.
[14] H. Ferdinande, N. K. Sherman, K. H. Lokan, and C. K. Ross, Can. J. Phys. **55**, 428 (1977).